

A fully coupled opto-electro-thermal model to investigate silicon solar cells under real operating conditions

Jérémy Dumoulin^{1,*} , Emmanuel Drouard² , and Mohamed Amara^{1,**}

¹ Univ Lyon, INSA Lyon, CNRS, ECL, UCBL, CPE Lyon, INL, UMR5270, 69621 Villeurbanne, France

² Univ Lyon, ECL, INSA Lyon, CNRS, UCBL, CPE Lyon, INL, UMR5270, 69130 Ecully, France

Received: 8 June 2022 / Received in final form: 26 July 2022 / Accepted: 2 August 2022

Abstract. In this work, a fully coupled opto-electro-thermal model for crystalline silicon solar cells is presented. Based on a detailed set of material properties, the developed model allows us to predict and analyse the solar cell behaviour under real operating conditions in a standalone framework. The results show the potential of our model to study the influence of the cell design on its real operating performance, thus giving a new opportunity for silicon solar cell optimisation. Specifically, the doping level is found to impact both the operating temperature and the temperature coefficient, showing that two cells with the same power conversion efficiency in standard test conditions can have a very different efficiency under real operating conditions. We also demonstrate the model capability to assess in detail the influence of environmental conditions, such as the solar spectrum, which also impacts the temperature coefficient. As the latter is not required by our material-based approach but is a simulation output, this work opens the way to more reliable outdoor prediction. Moreover, the various perspectives and challenges associated with the proposed detailed multiphysics simulation of solar cells are discussed, providing important guidelines for future studies.

Keywords: Silicon solar cell / real operating conditions / multiphysics modelling / thermal management / finite-element simulation

1 Introduction

Silicon solar cells are designed to efficiently absorb a large part of solar photons but for most of them convert only a limited proportion of sunlight into electricity. Under real operating conditions (ROC) solar cells therefore operate at much higher temperatures [1] than in standard test conditions (STC), i.e., with the reference AM 1.5 spectrum under 1000 W.m^{-2} and a cell temperature fixed to 25°C . However, this overheating reduces at first the power conversion efficiency as well as the overall photovoltaic (PV) module lifetime [2]. For commercial crystalline silicon (c-Si) devices, the relative efficiency loss is typically between 0.3 and 0.5% for every 1°C increase [3,4]. This combined loss of performance and lifetime significantly reduces the energy yield [5]. Thus, there is a need to develop solar cell models that allow to accurately address these thermal effects in order to both make reliable outdoor prediction and tackle the elevated temperature issues.

As illustrated in Figure 1, the performance of solar cells under ROC involves a complex interplay between their optical, electrical and thermal properties. Current modelling approaches are therefore often based on empirical correlations [6] or on global heat balance analysis [7–9]. Although the latter approach is constructed on a physical basis, it generally relies on empirical device parameters such as the temperature coefficients in [8]. Little work has been done to predict the thermal and electrical behaviour directly using material properties as input parameters for simulation. The first milestone for silicon cells was set in 2006 with the work of Vaillon et al. [10]. However, the heuristic model used for the heat sources did not include some important thermoelectric self-heating phenomena such as the Joule and Peltier effect. Using the rigorous heat treatment in semiconductors developed by Lindelfelt [11], our previous work [12] has shown the importance of using a complete set of heat sources to consistently describe the electro-thermal coupling. However, the electrical model of reference [12] is based on a depletion zone approximation and the optical part is treated analytically. These two assumptions severely limit the model’s ability to capture the behaviour of real silicon devices. Since then, Shang et al. [13] has proposed a model for GaAs (Gallium

* e-mail: jeremy.dumoulin@insa-lyon.fr

** e-mail: mohamed.amara@insa-lyon.fr

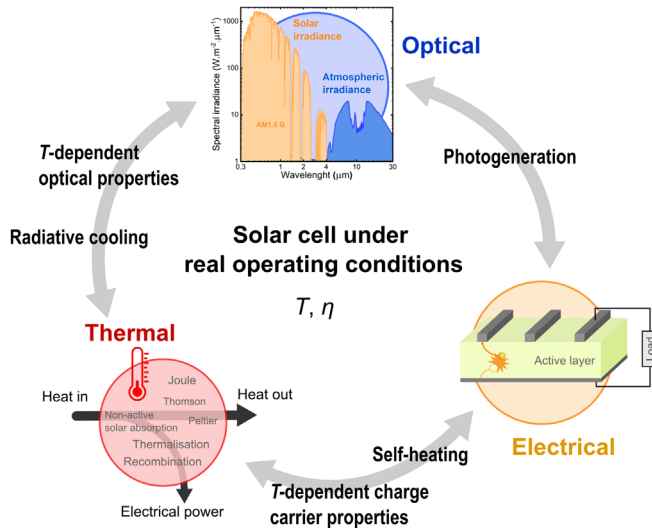


Fig. 1. The three physical modules and their main interconnections that rule the behaviour of solar cells under real operating conditions. Solar absorption and radiative heat exchange with the atmosphere govern the photogeneration of charge carriers as well as radiative cooling, thus requiring a very broadband optical calculation. Heat generation in the solar cell is the result of self-heating mechanisms (Joule, Peltier, Thomson effect, non-radiative recombinations, thermalisation) as well as solar absorption in non-active regions. The temperature-dependent optical and electrical properties introduce an additional coupling between the different physics.

Arsenide) cells that include complete semiconductor carrier transport equations and the calculation of the optical properties by electromagnetic simulations. Similar studies have been used very recently to study perovskite and CZTS (Copper Zinc Tin Sulfide) structures [14,15]. However, the latter three works do not incorporate detailed material parameters as required for c-Si cells [16], such as the temperature-dependent Klaassen mobility model [17]. Furthermore, they do not achieve a full coupling between the optical and electro-thermal physics which is found to be of great importance.

In this paper, we present a fully coupled opto-electro-thermal (OET) model of c-Si solar cells to calculate the temperature and the electrical output in given environmental conditions. The COMSOL Multiphysics software is used to solve the problem using the finite element method. The simulation solves for the complete Maxwell's and carrier transport equations, together with a detailed thermal model which includes all the main self-heating processes occurring in the solar cell (Joule heating, thermalisation, charge carrier recombination, Peltier effect, Thomson cooling) and solar absorption in non-active layers. Detailed input sets are used for all physical modules, such as a temperature-dependent complex refractive index of c-Si which is found to be crucial for accurate simulation results. Radiative and convective

cooling are also implemented. Notably, the former is treated in a free-standing way by computing the optical properties up to mid-infrared wavelengths.

The paper starts with a description of the physical model and the simulation procedure used to solve the coupled OET equations. Then, we investigate the importance of our fully coupled approach by comparing different coupling scenarios on a benchmark c-Si cell. Following that, we unveil the potential of our model to study the influence of the cell design on its real operating performance, thus offering a new route for silicon solar cell optimisation. This is illustrated by showing the influence of the doping level on the electrical and thermal behaviour. We also explore the influence of the solar spectrum on the real operating performance of the solar cell, showing that our model allows for an in-depth investigation of the impact of the environmental conditions. Although a simple solar cell is considered for the sake of illustration, the presented model could be straightforwardly extended to handle more complex designs by means of a higher computational cost. In this respect, the last section aims to provide a clear vision about the prospects and challenges associated with such detailed multiphysics simulation. This work paves the way for a standalone material-based simulation of the opto-electro-thermal behaviour of silicon solar cells under real operating conditions.

2 Methods

2.1 Physical models

The various governing equations are implemented using the Wave Optics, Semiconductor, and Heat Transfer in Solids modules of COMSOL Multiphysics. As mentioned in the introduction, these mainly originate from the work of Couderc et al. [12] and Shang et al. [13]. Here, we briefly review the equations and the underlying physics. We also present the various boundary conditions and environmental parameters used in the present paper.

2.1.1 Optical model

The optical absorption is calculated by solving the Helmholtz equation in the frequency domain

$$\nabla \times (\nabla \times \mathbf{E}) = k_0^2 \underline{n}^2 \mathbf{E} \quad (1)$$

where \mathbf{E} is the electric field, k_0 the free space wavenumber, and \underline{n} is the complex refractive index of the solar cell materials. The output is the local electromagnetic field, which is then used to compute the optical generation rate G of electrons and holes

$$G = \int_{E_g}^{\infty} g_E(E) dE \quad (2)$$

with E_g being the band gap energy of silicon, and $g_E(E)$ the optical generation profile for every excitation energy. As for the boundary conditions, Floquet periodic conditions are

used laterally whereas the top and bottom sides of the simulation domain are surrounded by perfectly matched layers.

2.1.2 Electrical model

The electrical output of the solar cell is obtained by solving the Poisson equation together with the steady-state current continuity equations using the electron (J_n) and hole (J_p) drift-diffusion current densities

$$\Delta\Phi = -\frac{q}{\varepsilon}(p - n + C) \quad (3)$$

$$\frac{-\nabla \cdot \mathbf{J}_p}{q} = G - R \quad (4)$$

$$\frac{\nabla \cdot \mathbf{J}_n}{q} = G - R \quad (5)$$

$$\frac{\mathbf{J}_n}{q} = n\mu_n \nabla E_c + D_n \nabla n - nD_n \nabla \ln(N_c) + nD_{n,th} \nabla \ln(T) \quad (6)$$

$$\frac{\mathbf{J}_p}{q} = p\mu_p \nabla E_v - D_p \nabla p + pD_p \nabla \ln(N_v) - pD_{p,th} \nabla \ln(T). \quad (7)$$

Here, Φ denotes the electrostatic potential, q the electron charge, ε the permittivity, n (p) the electron (hole) concentration, C the impurity charge concentration, μ_n (μ_p) the electron (hole) mobility, E_c (E_v) the conduction (valence) band energy, D_n (D_p) the electron (hole) diffusion coefficient, N_c (N_v) the effective conduction (valence) band density of states, $D_{n,th}$ ($D_{p,th}$) the thermal diffusion coefficient for electrons (holes), and T the temperature. It should be noted that these equations also take into account non-isothermal effects (last term of Eqs. (6) and (7)), which is not usually the case in the simulation of solar cell devices [18,19].

As for charge carrier generation and recombination, we consider optical generation G and non-radiative recombination R arising from Auger and Shockley-Read-Hall (SRH) mechanisms. Radiative recombination are not taken into account because of their minor role in silicon-based devices. For charge carrier collection we assume perfect ohmic contacts on both sides of the device.

2.1.3 Thermal model

The temperature distribution through the device is computed with the heat transfer in solids interface, which solves for the stationary heat equation

$$\nabla \cdot (-\kappa(T) \nabla T) = H \quad (8)$$

where κ is the thermal conductivity, and H the local heat source. In the non-active layers of the solar cell (metallic contacts, dielectric coatings) and for above band gap wavelengths the electromagnetic power dissipation is used

as the heat source. In the active layer (i.e., the crystalline silicon layer), the heat source is the sum of four bulk heat processes ($H = H_{th} + H_{Joule} + H_{NRR} + H_{Tho}$)

$$H_{th} = \int_{E_g}^{\infty} (E - E_g - 3k_b T) g_E(E) dE \quad (9)$$

$$H_{Joule} = \mathbf{J} \cdot (-\nabla \phi) \quad (10)$$

$$H_{NRR} = (E_g + 3k_b T) R \quad (11)$$

$$H_{Tho} = \nabla \cdot (\pi_n \mathbf{J}_n - \pi_p \mathbf{J}_p) \quad (12)$$

with H_{th} the thermalisation heat source, H_{Joule} the Joule heating, H_{NRR} the non-radiative recombination heating, H_{Tho} the Thomson effect, \mathbf{J} the total current density from electrons and holes, k_b the Boltzmann constant, π_n (π_p) the Peltier coefficients for electrons (holes). These expressions originate from the theoretical work of Lindefelt [11]. The latter has developed a rigorous framework for the treatment of heat in semiconductor devices by deriving the various source terms directly from the Boltzmann transport equation and the fundamental relations of linear irreversible thermodynamics.

At the boundary of the active layer we also account for surface recombination [13] and Peltier effect at both the n-type ($H_{Peltier,n}$) and the p-type ($H_{Peltier,p}$) contacts [13,20]

$$H_{Peltier,n} = J(E_c - E_{Fn} + 1.5k_b T) \quad (13)$$

$$H_{Peltier,p} = J(E_v - E_{Fp} + 1.5k_b T) \quad (14)$$

where E_{Fn} is the quasi-Fermi level for electrons and E_{Fp} the quasi-Fermi level for holes.

Finally, as boundary conditions for the entire device, we include convective (H_{con}) and radiative (H_{rad}) heat transfer at both the front and rear sides

$$H_{con} = h_c(T - T_a) \quad (15)$$

$$H_{rad} = \varepsilon \sigma (T^4 - T_a^4) \quad (16)$$

where T_a is the ambient temperature, σ is the Stefan-Boltzmann constant, h_c is the convective heat transfer coefficient, and ε the total hemispherical emissivity. Heat conduction with the front side contact is not taken into account.

2.2 Reference solar cell structure and environmental parameters

The simulated reference solar cell (Fig. 2) is made of a 10 μm thick p-doped crystalline silicon substrate. Charge carrier separation is realised with an n^+ front side emitter and a p^+ back surface field (BSF). A silicon nitride coating and a full-area aluminium layer are also added for enhanced solar absorption. The various material parameters and models are listed in Table 1. For the sake of simplicity, front contacts are evaluated using a numerical shading

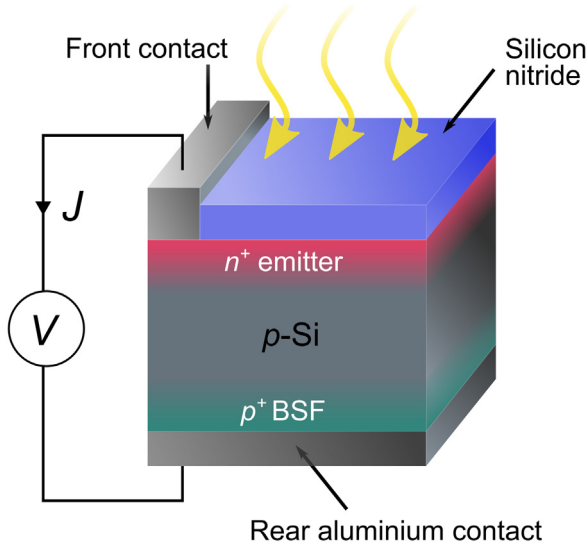


Fig. 2. Schematic of the silicon solar cell considered in this work.

factor in the optical model and the electro-thermal model is solved assuming 1D charge carrier transport. The solar cell has a simulated efficiency $\eta = 14.68\%$ (open circuit voltage $V_{oc} = 671$ mV, short-circuit current $J_{sc} = 26.03$ mA.cm⁻²) under standard test conditions. The low short-circuit current compared to the maximum value of about 44 mA.cm⁻² is due to the lack of light trapping through surface texturing and so large reflectance.

As the source of light, we use the standard AM 1.5 solar spectrum, except for Section 3.3, where the effect of the solar spectrum is investigated. Note that we considered normal incidence only, so that for a planar structure the optical response is independent of the polarisation state of the incident plane waves. The convective heat transfer coefficient is taken equal to 5 W.m⁻².K⁻¹ for the front side and 2 W.m⁻².K⁻¹ for the rear side. The total hemispherical emissivity ϵ is estimated according to Kirchhoff's law, by computing the infrared absorptivity through wave optics simulation [34]. Any angular and temperature dependence is neglected in this work for simplicity. The radiative heat transfer on the rear side is also not considered due to the low emissivity of aluminium [35].

2.3 Coupling procedure

The equations governing the OET behaviour are coupled together through an iterative procedure:

- 1) The optical part is calculated by summing the contribution of each wavelength contained in the incident solar spectrum.
- 2) The electrical and thermal parts are solved self-consistently using the output of step 1).

These two steps are repeated until the absolute temperature difference between two iterations is smaller than a target value (0.05 °C in this work). In the first iteration, a constant temperature distribution (equal to the ambient temperature T_a) is used for the optical calculation. A flow chart is provided in the Appendix, representing the iterative

Table 1. Input parameters and models for the simulated reference solar cell.

	Cell design
Silicon	Thickness 10 μm , p-type (2.10^{16} cm ⁻³)
n^+ emitter	Gaussian doping profile (2.10^{19} cm ⁻³ peak doping, 100 nm decay length)
p^+ BSF	Gaussian doping profile (2.10^{19} cm ⁻³ peak doping, 100 nm decay length)
Front coating	Silicon nitride, thickness 70 nm
Rear contact	Full-area aluminium, thickness 300 nm
Front contact shading	4%
Silicon nitride	
Refractive index	Vogt [21] up to 1.7 μm , Kischkat [22] beyond
Thermal conductivity	2.2 W.m ⁻¹ .K ⁻¹ [23]
Silicon	
Complex refractive index	Green [24] for wavelengths below 1.2 μm , Fu [25] above ¹
Thermal conductivity	Glassbrenner [26]
Peltier coefficients	$\pi_n = \pi_p = 0.5$ V [27]
Carrier statistics	Fermi-Dirac
Ionisation of dopants	Complete
Intrinsic carrier density	Couderc [28]
Band gap energy	Pässler [29]
Carrier mobility	Klaassen [17]
Auger recombination	Niewelt [30]
SRH lifetime	30 μs
Aluminium	
Refractive index	Rakic [31]
Thermal conductivity	243.0 W.m ⁻¹ .K ⁻¹ [32]

procedure in more detail. The COMSOL direct solver called MUMPS is used for the three physical modules.

3 Results and discussions

Figure 3 shows the two main outputs of the fully coupled model, namely the current–voltage characteristic and the solar cell temperature under ROC. As compared to STC, the operating temperature under ROC is not arbitrarily set to 25 °C but depends on the thermal equilibrium state reached by the solar cell, which itself depends on the set of environmental condition (solar spectrum, ambient temperature T_a , convective heat transfer coefficient h), the solar cell

¹ The Drude model used in reference [25] has been replaced by the model of Basu et al. [33] to better account for free carrier absorption in heavily doped regions.

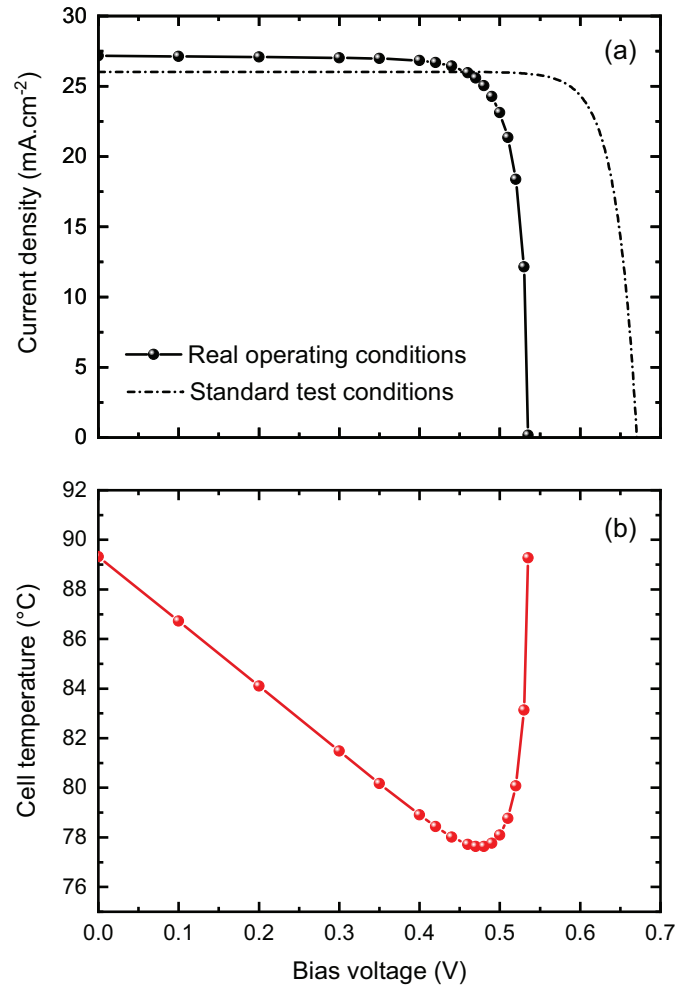


Fig. 3. Solar cell current–voltage (a) and temperature–voltage (b) characteristics simulated in real operating conditions. The current–voltage characteristic under STC ($T = 25\text{ °C}$ regardless of the bias voltage) is also shown as a dotted line in the upper figure.

design, and the bias voltage V [28]. Thus, the operating temperature in ROC is much higher than 25 °C . As a consequence, the current–voltage characteristic shows a decrease in V_{oc} and a slight increase in J_{sc} , which are two well-known consequences of increasing cell temperature [36,37]. Moreover, the effect of the bias voltage on the cell temperature can be observed. Indeed, in agreement with previous simulation results [28], the lowest cell temperature is reached near the maximum power point while the temperature is highest at the short-circuit and the open-circuit voltage. This illustrates that the model is able to capture the essential phenomena observed on the device scale from material-based inputs.

To account for all these, attention must be paid to the coupling between the three physical modules. In the following, we first compare different coupling scenarios to highlight the importance of our fully coupled approach. We then show how this fully coupled model could allow us to study the influence of the solar cell design and the environmental conditions on its performance under ROC. For example, we will see how these two aspects can change the temperature sensitivity coefficient. Thanks to our material-based approach, the latter can be calculated and

analysed in a standalone way. Finally, we discuss the numerous perspectives that emerge from this work and the associated challenges.

3.1 The importance of a fully coupled simulation

Figure 4 illustrates the impact of different coupling scenarios on the cell temperature and short-circuit current, using the environmental conditions given in Methods section. In fact, the optical, thermal and electrical material properties of solar cells are strongly coupled together in the active layer. In this section, we therefore propose to study how the level of coupling quantitatively impacts the model output (cf., flow chart of the different coupling scenarios in the Appendix). The first scenario of Figure 4 (“w/o coupling”) corresponds to the case where there is no coupling, meaning that the operating conditions are those of the standard test conditions and therefore the temperature is equal to 25 °C .

In the second scenario (“w/ET coupling only”), only the electrical and thermal modules are coupled meaning that there is no feedback of these latter to the optical response (i.e., the complex refractive index at ambient temperature is used) as done in previous multiphysics simulation work

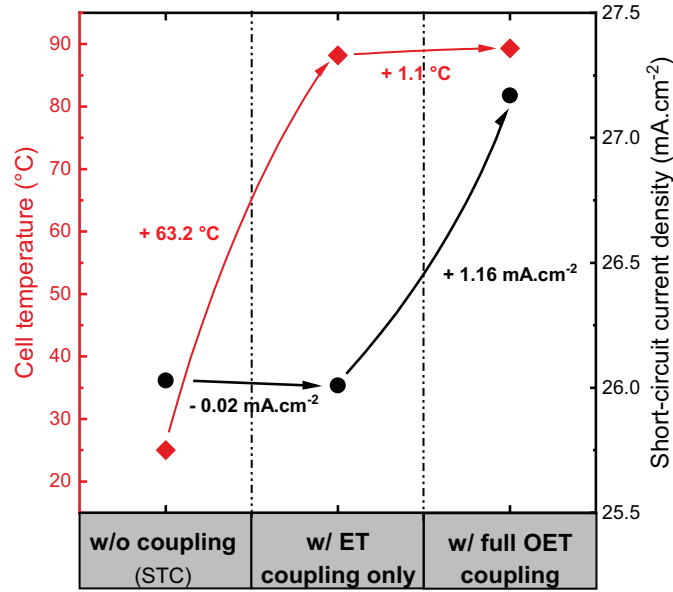


Fig. 4. Current density and cell temperature under short-circuit conditions in different coupling scenarios. In the first scenario (“w/o coupling”), the solar cell is operating under STC (its temperature is set to 25 °C). In the second scenario (“w/ET coupling only”), the thermal module is coupled to the electrical module, but the optical response is calculated assuming a complex refractive index equal to 25 °C. In the third scenario (“w/full OET coupling”), all the three physical modules are coupled together.

Table 2. Heat sources and heat sinks of the reference cell at short-circuit condition for the electro-thermal (ET) and the opto-electro-thermal (OET) coupling scenarios.

	Heat sources and heat sinks (W.m ⁻²)	
	w/ET coupling only	w/full OET coupling
Joule	291.7	304.6
Thermalisation	224.0	227.2
Non-active absorption	70.7	63.9
Peltier	20.6	21.7
Non-radiative recombination	17.6	19.6
Convection	442.35	450.2
Radiation	173.7	177.8
Thomson	8.55	9.0
TOTAL	624.6	637.0

[13–15]. Due to the many heat sources present in the cell, this leads to a much higher temperature than the ambient temperature (+63.2 °C). As depicted in Table 2, the most important heat source is the Joule effect, which occurs mainly near the p-n junction. The second heat source is thermalisation, which occurs near the front surface due to the absorption profile of silicon. Thirdly, solar absorption in the non-active materials also plays an important role in the heating of the cell. It mostly arises from the backside metallic contact because many solar photons are not fully absorbed after a single pass through 10 μm of silicon. The Peltier effect at electrical contacts also accounts for a small fraction of the total heating.

The third scenario (“w/full OET coupling”) corresponds to the complete coupling achieved in this work. This coupling appears to be necessary to account for the increase

in J_{sc} (+1.16 mA.cm⁻²) with temperature mentioned earlier. In the second scenario, a slight decrease in J_{sc} (-0.02 mA.cm⁻²) is even observed due to the lower mobility of the charge carriers at higher temperature. This effect is outbalanced by the temperature dependence of the complex refractive index of c-Si enabled in the third scenario. In fact, the band gap energy decreases as the temperature rises, resulting in more band-to-band solar absorption. The absorption profile of the cell at different temperatures given in the Appendix shows this effect in more detail. This causes the temperature to increase even more (+1.1 °C) and slightly changes the distribution of heat sources and sinks. Especially Joule and thermalisation heating are more pronounced than in the second scenario due to a higher electric current and more photogenerated carriers, respectively. The small decrease in non-active

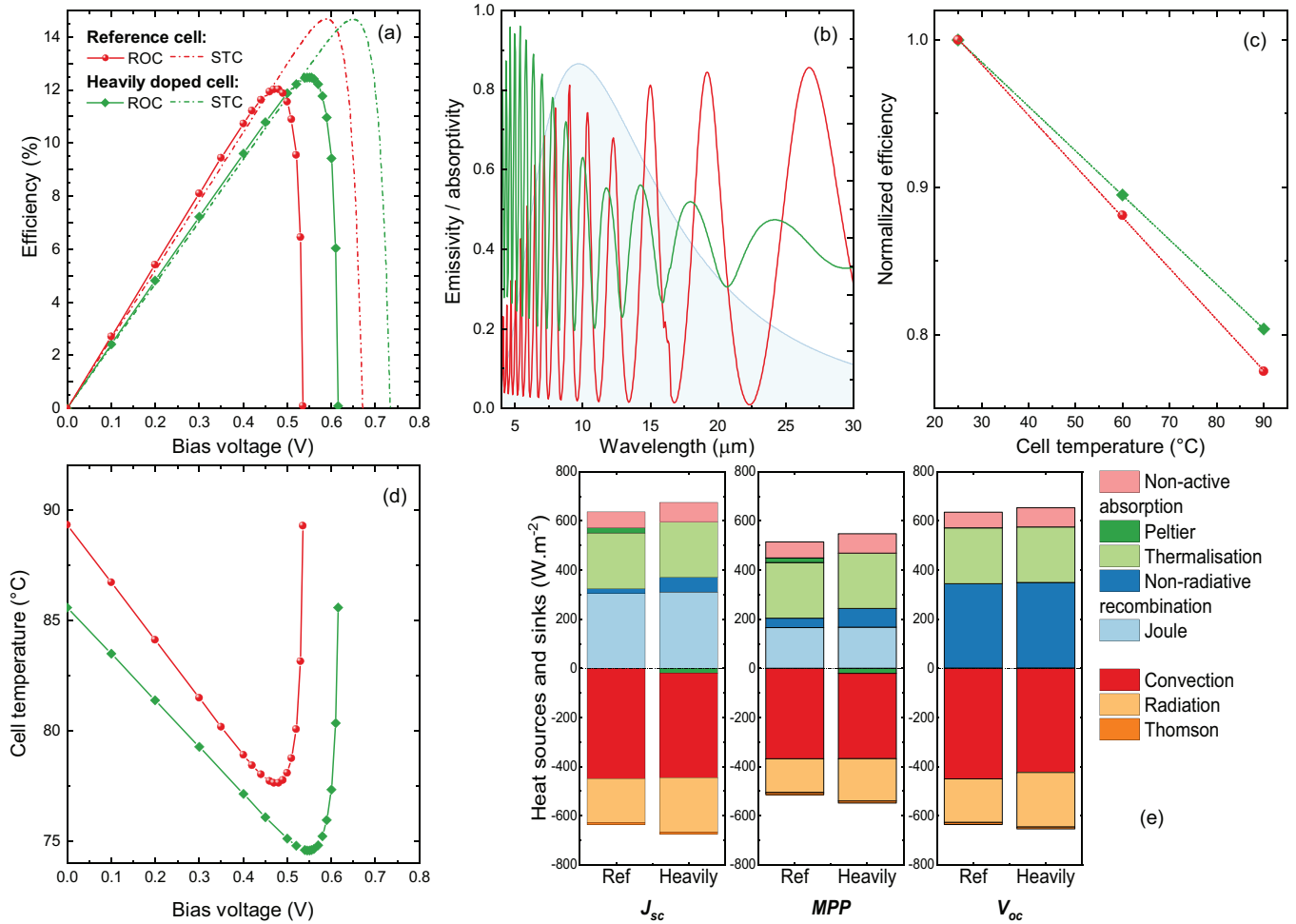


Fig. 5. (a) Power conversion efficiency of the two cells (reference in red and highly doped in green) under standard test conditions (dotted lines) and under real operating conditions (solid lines). (b) Spectral absorptivity under normal incidence of the two solar cells (reference cell in red and heavily doped cell in green), which is the ratio of the absorbed to the incident solar power. According to Kirchhoff’s law of radiation, the absorptivity is equal to the spectral emissivity, which is the ratio of the radiation emitted to the radiation emitted by a blackbody at a given wavelength. The emission spectrum of the blackbody at 25 °C is shown in the light blue. (c) Normalised efficiency (η/η_{stc}) as a function of solar cell temperature, from which the temperature coefficient β can be extracted by linear fitting. (d) Temperature-voltage characteristic. (e) Heat sources and sinks of the two cells at three specific operating points: the short-circuit (J_{sc}), the maximum power (MPP), and the open-circuit (V_{oc}).

absorption is due to the band gap shift, which leads to less absorption in the rear aluminium. As we can see, this example highlights the importance of a full OET coupling to accurately study the electrical and thermal output of the solar cell.

3.2 Influence of the solar cell design

The developed model allows an in-depth analysis of the influence of the solar cell design on its behaviour under real operating conditions. Here, we focus on the influence of the doping level. For this purpose, we consider a cell with a higher doping level ($2.6 \times 10^{18} \text{ cm}^{-3}$ for the base, $9 \times 10^{19} \text{ cm}^{-3}$ peak doping for the emitter and the BSF) than the reference cell, referred to the “heavily doped cell” in the following. As can be seen in Figure 5a, both solar cells exhibit the same power conversion efficiency (14.68% for the reference cell, 14.67% for the heavily doped

cell) under STC. However, under ROC, the heavily doped cell has a better efficiency (12.48%) than the reference cell (12.03%).

One reason behind this difference is the lower operating temperature induced by the heavily doped absorber, as depicted in Figure 5d. Indeed, a higher doping level leads to more absorption by free charge carriers in the mid-infrared spectral range [33,25]. Therefore, as stated by Kirchhoff’s law, the heavily doped cell exhibits a higher spectral emissivity (Fig. 5b). The result is a hemispherical ϵ emissivity equal to 0.45 for the heavily doped cell, against 0.33 for the reference cell. From Figure 5e, it should be noted that the higher doping level also leads to increased non-radiative recombination ($+41 \text{ W.m}^{-2}$ at short-circuit) and more non-active solar absorption ($+14 \text{ W.m}^{-2}$ at short-circuit). This mitigates the impact of thermal emissivity on temperature. Nevertheless, the heavily doped cell operates about 2 °C lower than the reference cell

mostly due to the high sensitivity of the operating temperature to the radiative cooling heat sink. The other reason for the difference under ROC is the better temperature sensitivity of the heavily doped cell. The temperature sensitivity is generally described through the temperature coefficient [38]

$$\eta(T) = \eta_{stc}[1 - \beta(T - T_{stc})] \quad (17)$$

where η_{stc} and T_{stc} are respectively the efficiency and the cell temperature in standard test conditions ($T_{stc} = 25^\circ\text{C}$). The value of β can be calculated either from the I - V curves at different temperatures (Fig. 5c), or directly by comparing the solar cell efficiency under real conditions with that under standard conditions. For the two designs considered here, both methods lead to a temperature coefficient equal to $0.34\%/^\circ\text{C}$ for the reference cell and $0.30\%/^\circ\text{C}$ for the heavily doped cell. Indeed, the doping level is known to increase the open-circuit voltage [39] which in turn decreases (in absolute value) the temperature coefficient [36].

Finally, it is interesting to note how the cell design may change the energy distribution between the different heat sources as seen on Figure 5e. The most notable is the Peltier effect, which changes from a heat source to a sink for the heavily doped cell. In this case, near the contacts, the electron (hole) quasi-Fermi level lies higher in the conduction (valence) band due to the elevated surface doping. From equations (13) and (14), in this configuration, the Peltier effect leads to heat extraction because the absolute difference $E_c - E_{Fn}$ at the n-type contact (and $E_v - E_{Fp}$ at the p-type contact) is greater than $1.5k_bT$ (cf., band diagram in the Appendix). Figure 5e also confirms that the radiative heat sink of the heavily doped cell is larger than that of the reference cell, due to its higher thermal emissivity.

3.3 Influence of environmental conditions

In addition to the influence of the cell design, our model allows us to study in detail the impact of the environmental conditions on the solar cell performance. Here, we propose to investigate the effect of the air mass which is a major variability factor of the terrestrial solar spectra. In order to do so, we compare the model output for two different solar cell spectra (the standard AM 1.5G spectrum and a AM 3G spectrum). The AM 3G spectrum was simulated using the SMARTS 2.9.5 software [40], with the same set of parameters given in reference [12].

Figure 6 shows the current-voltage characteristic of the reference solar cell under both spectra. When the cell temperature is set to 25°C , the J_{sc} and therefore the V_{oc} are lower for the AM 3G spectrum than for the AM 1.5G spectrum. This is no longer the case under ROC, where the V_{oc} under the AM 3G spectrum is higher than under the AM 1.5G spectrum. This is due to the lower cell temperature at V_{oc} (68.7°C under the AM 3G spectrum, 89.3°C under the AM 1.5G spectrum). This lower temperature is caused, on the one hand, by the lower irradiance and, on the other hand, by the better spectral match between the cell and the AM 3G spectrum, which

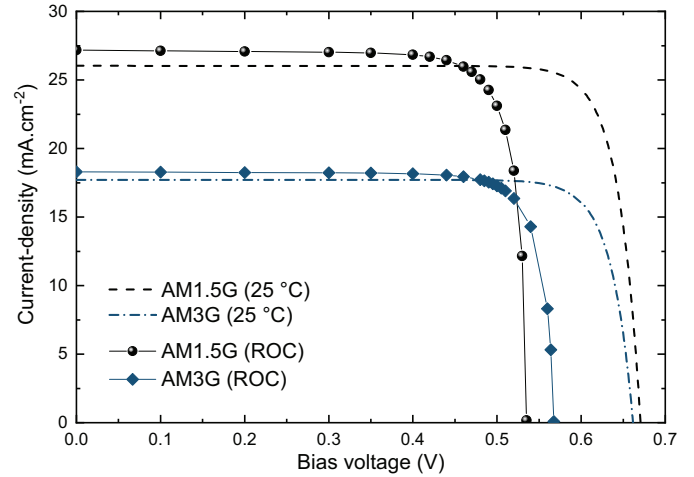


Fig. 6. Current-voltage characteristic of the reference cell under AM 1.5G and AM 3G spectra. The dashed lines correspond to a fixed cell temperature (25°C) whereas the solid lines correspond to the current-voltage characteristic under ROC.

has a lower fraction of high energy photons. Under ROC, this results in a better efficiency under the AM 3G spectrum ($+0.71\%$).

It is also noteworthy that the efficiency under the AM 3G spectrum is different from that estimated using the temperature coefficient calculated in Section 3.2. With the temperature coefficient $\beta = 0.34\%/^\circ\text{C}$ and a temperature at MPP equal to 59.9°C , the efficiency we expect with equation (17) is 12.94% . Nonetheless, the efficiency under ROC is 12.74% . In fact, the temperature sensitivity depends on the incident spectrum [38,41], even though this property is often not taken into account to predict the solar cell efficiency under ROC. The resulting errors might propagate and have a significant impact on, for example, the annual energy yield analysis. Our model avoids this difficulty because it does not require a temperature coefficient as an input. Nevertheless, it allows us to predict the latter and, if needed, could therefore also be used to feed energy yield simulation approaches with a spectrum-dependent β .

3.4 Future prospects and challenges

This paper provides a baseline model to study the behaviour of c-Si solar cells under real operating conditions. This type of material-based approach can be used to address a broad scope of scientific topics covering: (1) The influence of the solar cell design (cf., Sect. 3.2); (2) The role of environmental conditions (cf., Sect. 3.3). Put together, this paves the way for solar cell optimisation with thermal criteria as well as for accurate prediction of the OET behaviour in given environmental conditions. We note further that the proposed model could be set up to simulate other devices than c-Si solar cells, only requiring a change in the cell design and the material parameters used as inputs. Moreover, the model offers the opportunity to study thermal mitigation strategies such as radiative cooling [42] in a standalone simulation. By adding fluid dynamics simulations, it would also be possible to predict convective heat exchange from wind speed and

installation conditions [43]. Finally, we believe that this model can serve as a core model to evaluate the behaviour of an entire solar module or to perform energy yield estimates [44]. These perspectives are accompanied by major challenges, both in terms of physical modelling and numerical simulation.

As far as multiphysics modelling is concerned, the biggest challenge is to choose the right assumptions for the different physics. This will constrain the complexity and the accuracy of the simulation. One should note that this difficulty is twofold, because it concerns both the modelling of the solar cell and its surrounding environment. For example, in this work, we have treated thermal radiation as a boundary condition but it has been suggested that a participating media approach may be more accurate [1]. As shown in Section 3.1, special attention should also be paid to the degree of coupling. Another concern is about material properties, which are not always readily available. Notably, there is a need for temperature-dependent refractive index values up to the mid-infrared. Even for crystalline silicon only very few models are available [25,33]. Simulation results also need to be compared with experiments. This might be challenging, because environmental conditions can be difficult to manage and also because of the great model complexity. Therefore, our study strongly supports experimental investigation under controlled environmental conditions and a thorough validation of the various building blocks of the model.

The numerical challenges mainly relate to the computational effort associated with the model. The first obstacle originates from the relatively large device thickness compared to the solar spectrum wavelengths. As the thickness increases, so does the number of mesh elements required for the optical simulation. The associated computational cost would therefore be quite significant if our model is used to evaluate, for example, the OET behaviour of a solar module. This is also the case for solar cell architectures that require two- or three-dimensional processing. This issue might be solved by implementing computational cost reduction strategies, such as adopting a multi-scale approach [45,46]. As for using our model to feed simulations for energy yield estimations, this requires quick and easy access to the simulation outputs. This is usually done by using the outputs of the material-based model to create a surrogate model, suitable for the device scale (e.g. a diode model for the electrical part). The possible drawback of this approach is a loss of accuracy and generality. A promising way to overcome this problem might be to employ some recently developed machine learning algorithms [47].

4 Conclusion

This study has presented a fully coupled opto-electro-thermal model for crystalline silicon solar cells operating in real environmental conditions. Based on detailed governing equations and material parameters for the three physical modules, it enables us to predict the electrical output and the temperature of the solar cell by using material-based parameters as the only input. The thermal physics includes

all the thermoelectric self-heating processes as well as solar absorption in non-active layers, the latter having been found to be significant for the solar cell considered in this work. A detailed comparison between different coupling scenarios revealed the importance of our fully coupled approach to properly account for the temperature dependence of the optical properties of c-Si.

The results unveiled the potential of our model to study the influence of the solar cell design and the environmental conditions on the solar cell performance under ROC. First, depending on the doping level, we have shown that two solar cells with the same power conversion efficiency under STC can exhibit different efficiencies (about 4% relative difference for the considered environmental conditions) under ROC. The underlying reason was found to be twofold: (1) Different cell temperatures due to different thermal emissivities; (2) Different temperature coefficients attributed to the increase in open-circuit voltage with the doping level. Secondly, our study shed light on the dependence of the temperature coefficient on the solar spectrum. This shows that our model can be used to study in detail the influence of environmental conditions, thus enabling more reliable predictions under ROC than models based on a single temperature coefficient calculated under the AM 1.5G spectrum.

For future work, the prospects and challenges of this study have also been discussed. The challenges relate to both the physical modelling and the numerical simulation. For the former, the challenges mainly concern the fine-tuning of the model to match the desired level of accuracy. As for the numerical challenges, they are related to the high computational cost when considering thick silicon devices or with two- or three-dimensional structures. Some promising pathways to overcome these limitations have been presented.

Appendix A: Multiphysics coupling scheme

The coupling procedure that has been used to solve for the fully coupled OET behaviour (“w/full OET coupling”) is represented as a flow chart in the upper part of Figure 6. The graph shows the two-step procedure for calculating the solar cell operating temperature T and the current density J , for a given bias voltage V . To obtain the current–voltage or temperature–voltage characteristic, this procedure has to be repeated between the short-circuit and open-circuit conditions. In the fully coupled scenario, the electrical and thermal models are coupled together in step 2, and the resulting temperature is then fed back to the optical model, until self-consistent convergence is reached.

Figure A.1 also illustrates the other two coupling scenarios that were studied in Section 3.1, namely the “w/o coupling” and the “w/ET coupling only” scenarios. For the “w/o coupling” scenario, we can see that the thermal module is not used, thus assuming an operating temperature equal to the ambient temperature for both the optical and the electrical parts. For the “w/o coupling” scenario, the thermal module is used, but the operating temperature is still equal to the ambient temperature for the optical part.

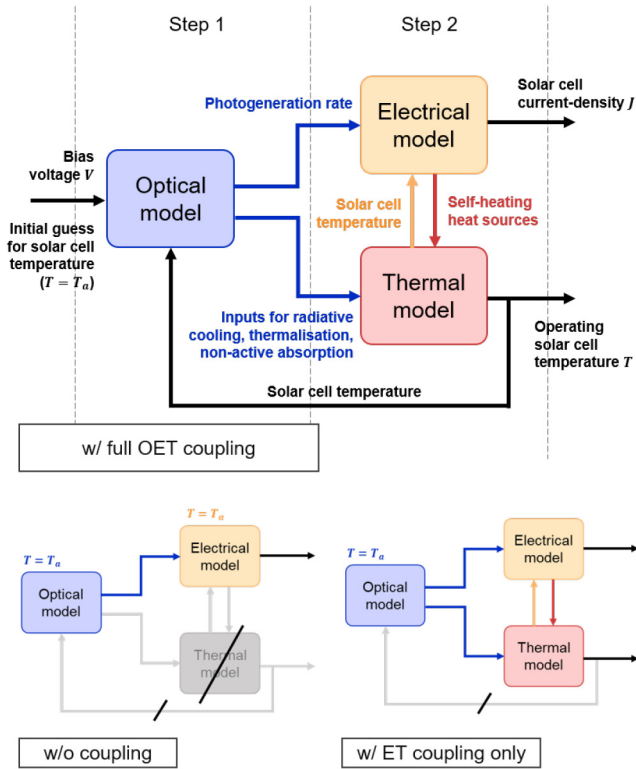


Fig. A.1. Flow chart of the different coupling scenarios studied in the present paper (“w/full OET coupling”, “w/o coupling”, “w/ET coupling only”). For the full OET coupling scenario, the main inputs, outputs, and interconnections are specified.

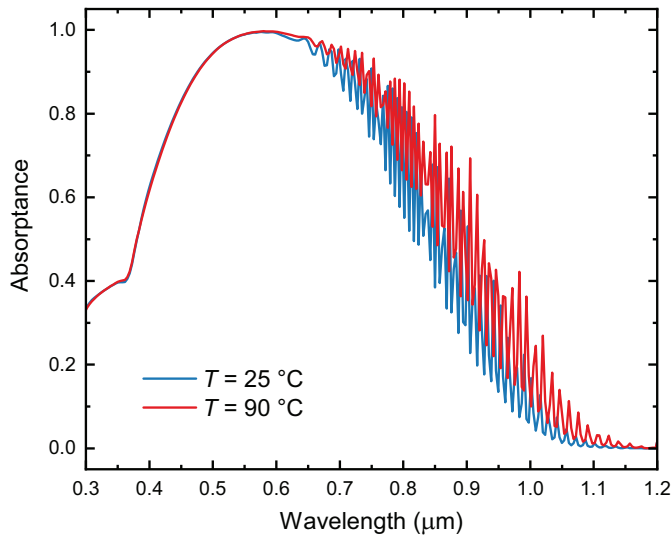


Fig. B.1. Absorbance of silicon (i.e., absorption in silicon nitride and aluminium are not shown) up to 1.2 μm calculated for the reference cell. The absorbance spectra is shown for two cell temperatures.

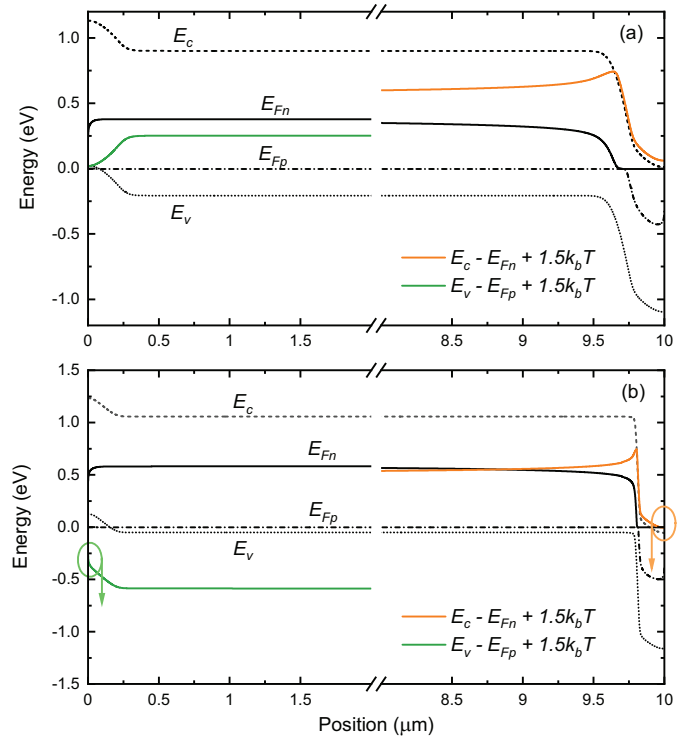


Fig. C.1. Band diagram of the reference solar cell (a) and the heavily doped cell (b), at short-circuit condition in a fully coupled scenario. The front side emitter is located at 10 μm while the rear side BSF is located at 0 μm . The values of $E_c - E_{F_n} + 1.5k_bT$ and $E_v - E_{F_p} + 1.5k_bT$ involved in the Peltier effect are shown in orange and green, respectively.

Appendix B: Impact of the cell temperature on optical absorption

The influence of the solar cell temperature on the absorbance of silicon is depicted in [Figure B.1](#). As a consequence of the temperature dependence of the complex refractive index of silicon [24], which mainly reflects the shift of the band gap energy, absorption increases with temperature. This, in turn, increases the photogeneration rate and thus the J_{sc} .

Appendix C: Solar cell band diagram

[Figure C.1](#) shows the band diagram of the reference solar cell and the heavily doped cell. The values of $E_c - E_{F_n} + 1.5k_bT$ and $E_v - E_{F_p} + 1.5k_bT$ involved in the Peltier effect are also depicted, showing that for the heavily doped cell they are negative at the surface, leading to heat extraction. Indeed, in this case, the absolute difference $E_c - E_{F_n}$ at the n-type contact (and $E_v - E_{F_p}$ at the p-type contact) is greater than $1.5k_bT$.

Author contribution statement

J. Dumoulin developed the COMSOL model and carried out the simulations. The supervision of the project was ensured by M. Amara and E. Drouard. As for the physical model, M. Amara largely contributed to set up the governing equations of the thermal model. The manuscript was written by J. Dumoulin. All the authors discussed the results and actively contributed to manuscript revisions.

References

1. L. Weiss, M. Amara, C. Ménézo, Impact of radiative-heat transfer on photovoltaic module temperature, *Progr. Photovolt.: Res. Appl.* **24**, 12–27 (2016)
2. A. Ndiaye, A. Charki, A. Kobi, C.M.F. Kébé, P.A. Ndiaye, V. Sambou, Degradations of silicon photovoltaic modules: a literature review, *Solar Energy* **96**, 140–151 (2013)
3. A. Virtuani, D. Pavanello, G. Friesen, Overview of temperature coefficients of different thin film photovoltaic technologies, in *Proc. 25th Eur. Photovoltaic Sol. Energy Conf. Exhib.* (2010), pp. 4248–4252
4. J. Haschke, J.P. Seif, Y. Riesen, A. Tomasi, J. Cattin, L. Tous, P. Choulat, M. Aleman, E. Cornagliotti, A. Uruena, R. Russell, F. Duerinckx, J. Champlaud, J. Levrat, A.A. Abdallah, B. Aïssa, N. Tabet, N. Wyrsh, M. Despeisse, J. Szlufcik, S. De Wolf, C. Ballif, The impact of silicon solar cell architecture and cell interconnection on energy yield in hot & sunny climates, *Energy Environ. Sci.* **10**, 1196–1206 (2017)
5. L. Xu, W. Liu, H. Liu, C. Ke, M. Wang, C. Zhang, E. Aydin, M. Al-Aswad, K. Kotsosvos, I. Gereige, A. Al-Saggaf, A. Jamal, X. Yang, P. Wang, F. Laquai, T.G. Allen, S. De Wolf, Heat generation and mitigation in silicon solar cells and modules, *Joule* **5**, 631–645 (2021)
6. E. Skoplaki, J.A. Palyvos, On the temperature dependence of photovoltaic module electrical performance: a review of efficiency/power correlations, *Solar Energy* **83**, 614–624 (2009)
7. A.D. Jones, C.P. Underwood, A thermal model for photovoltaic systems, *Solar Energy* **70**, 349–359 (2001)
8. O. Dupré, R. Vaillon, M.A. Green, A full thermal model for photovoltaic devices, *Solar Energy* **140**, 73–82 (2016)
9. W. Gu, T. Ma, M. Li, L. Shen, Y. Zhang, A coupled optical-electrical-thermal model of the bifacial photovoltaic module, *Appl. Energy* **258**, 114075 (2020)
10. R. Vaillon, L. Robin, C. Muresan, C. Ménézo, Modeling of coupled spectral radiation, thermal and carrier transport in a silicon photovoltaic cell, *Int. J. Heat Mass Transfer* **49**, 4454–4468 (2006)
11. U. Lindelfelt, Heat generation in semiconductor devices, *J. Appl. Phys.* **75**, 942–957 (1994)
12. R. Couderc, M. Amara, M. Lemiti, In-depth analysis of heat generation in silicon solar cells, *IEEE J. Photovolt.* **6**, 1123–1131 (2016)
13. A. Shang, X. Li, Photovoltaic devices: opto-electro-thermal physics and modeling, *Adv. Mater.* **29**, 1–8 (2017)
14. P. Saxena, N.E. Gorji, COMSOL simulation of heat distribution in perovskite solar cells: coupled optical-electrical-thermal 3-D analysis, *IEEE J. Photovolt.* **9**, 1693–1698 (2019)
15. S. Zandi, M. Jamshidi Seresht, A. Khan, N.E. Gorji, Simulation of heat loss in $\text{Cu}_2\text{ZnSnS}_4\text{Se}_x$ thin film solar cells: A coupled optical-electrical-thermal modeling, *Renew. Energy* **181**, 320–328 (2022)
16. A. Fell, K.R. McIntosh, P.P. Altermatt, G.J.M. Janssen, R. Stangl, A. Ho-Baillie, H. Steinke, J. Greulich, M. Müller, B. Min, K.C. Fong, M. Hermle, I.G. Romijn, M.D. Abbott, Input parameters for the simulation of silicon solar cells in 2014, *IEEE J. Photovolt.* **5**, 1250–1263 (2015)
17. D.B.M. Klaassen, A unified mobility model for device simulation—I. Model equations and concentration dependence, *Solid-State Electr.* **35**, 953–959 (1992)
18. D.A. Clugston, P.A. Basore, PC1D version 5: 32-bit solar cell modeling on personal computers, in *Conference Record of the IEEE Photovoltaic Specialists Conference* (1997), pp. 207–210
19. M. Burgelman, P. Nollet, S. Degraeve, Modelling polycrystalline semiconductor solar cells, *Thin Solid Films* **361**, 527–532 (2000)
20. M. Lundstrom, C. Jeong, *Near-equilibrium Transport: Fundamentals and Applications* (World Scientific, 2012)
21. M.R. Vogt, H. Holst, M. Winter, R. Brendel, P.P. Altermatt, Numerical modeling of c-Si PV modules by coupling the semiconductor with the thermal conduction, convection and radiation equations, *Energy Proc.* **77**, 215–224 (2015)
22. J. Kischkat, S. Peters, B. Gruska, M. Semtsiv, M. Chashnikova, M. Klinkmüller, O. Fedosenko, S. MacHulik, A. Aleksandrova, G. Monastyrskyi, Y. Flores, W. Ted Masselink, Mid-infrared optical properties of thin films of aluminum oxide, titanium dioxide, silicon dioxide, aluminum nitride, and silicon nitride, *Appl. Opt.* **51**, 6789–6798 (2012)
23. M. Von Arx, O. Paul, H. Baltes, Process-dependent thin-film thermal conductivities for thermal CMOS MEMS, *J. Microelectromech. Syst.* **9**, 136–145 (2000)
24. M.A. Green, Self-consistent optical parameters of intrinsic silicon at 300 K including temperature coefficients, *Solar Energy Mater. Solar Cells* **92**, 1305–1310 (2008)
25. C.J. Fu, Z.M. Zhang, Nanoscale radiation heat transfer for silicon at different doping levels, *Int. J. Heat Mass Transfer* **49**, 1703–1718 (2006)
26. C.J. Glassbrenner, G.A. Slack, Thermal conductivity of silicon and germanium from 3°K to the melting point, *Phys. Rev.* **134**, A1058 (1964)
27. H. Straube, J. Martin Wagner, O. Breitenstein, Measurement of the Peltier coefficient of semiconductors by lock-in thermography, *Appl. Phys. Lett.* **95**, 5–8 (2009)
28. R. Couderc, M. Amara, M. Lemiti, Reassessment of the intrinsic carrier density temperature dependence in crystalline silicon, *J. Appl. Phys.* **115**, 093705 (2014)
29. R. Pässler, Dispersion-related description of temperature dependencies of band gaps in semiconductors, *Phys. Rev. B* **66**, 1–18 (2002)
30. T. Niewelt, B. Steinhäuser, A. Richter, B. Veith-Wolf, A. Fell, B. Hammann, N.E. Grant, L. Black, J. Tan, A. Youssef, J.D. Murphy, J. Schmidt, M.C. Schubert, S.W. Glunz, Reassessment of the intrinsic bulk recombination in crystalline silicon, *Solar Energy Mater. Solar Cells* **235**, 111467 (2022)
31. A.D. Rakić, A.B. Djurišić, J.M. Elazar, M.L. Majewski, Optical properties of metallic films for vertical-cavity optoelectronic devices, *Appl. Opt.* **37**, 5271 (1998)

32. J.M. Lugo, A.I. Oliva, Thermal properties of metallic films at room conditions by the heating slope, *J. Thermophys. Heat Transfer* **30**, 452–460 (2016)
33. S. Basu, B.J. Lee, Z.M. Zhang, Infrared radiative properties of heavily doped silicon at room temperature, *J. Heat Transfer* **132**, 1–8 (2010)
34. T.L. Bergman, A.S. Lavine, F.P. Incropera, D.P. DeWitt, Fundamentals of heat and mass transfer, in *Fluid Mechanics and its Applications* (2015), Vol. 112, pp. 321–338
35. E.A. Estalote, K.G. Ramanathan, Low-temperature emissivities of copper and aluminum, *J. Opt. Soc. Am.* **67**, 39 (1977)
36. M.A. Green, General temperature dependence of solar cell performance and implications for device modelling, *Progr. Photovolt.: Res. Appl.* **11**, 333–340 (2003)
37. S. Chander, A. Purohit, A. Sharma, Arvind, S.P. Nehra, M.S. Dhaka, A study on photovoltaic parameters of mono-crystalline silicon solar cell with cell temperature, *Energy Rep.* **1**, 104–109 (2015)
38. D.L. Evans, Simplified method for predicting photovoltaic array output, *Solar Energy* **27**, 555–560 (1981)
39. J. Brody, A. Rohatgi, V. Yelundur, Bulk resistivity optimization for low-bulk-lifetime silicon solar cells, *Progr. Photovolt.: Res. Appl.* **9**, 273–285 (2001)
40. C.A. Gueymard, Parameterized transmittance model for direct beam and circumsolar spectral irradiance, *Solar Energy* **71**, 325–346 (2001)
41. O. Dupr e, R. Vaillon, M.A. Green, Physics of the temperature coefficients of solar cells, *Solar Energy Mater. Solar Cells* **140**, 92–100 (2015)
42. J. Dumoulin, E. Drouard, M. Amara, Radiative sky cooling of solar cells: fundamental modelling and cooling potential of single-junction devices, *Sustain. Energy Fuels* **5**, 2085–2096 (2021)
43. N. Dabaghzadeh, M. Eslami, Temperature distribution in a photovoltaic module at various mounting and wind conditions: a complete CFD modeling, *J. Renew. Sustain. Energy* **11**, 053503 (2019)
44. I. Marius Peters, T. Buonassisi, Energy yield limits for single-junction solar cells, *Joule* **2**, 1160–1170 (2018)
45. D. Alonso- lvarez, T. Wilson, P. Pearce, M. F uhrer, D. Farrell, N. Ekins-Daukes, Solcore: a multi-scale, Python-based library for modelling solar cells and semiconductor materials, *J. Comput. Electr.* **17**, 1099–1123 (2018)
46. S. Dahal, J. Waddle, M. Nardone, Multi-scale simulation of thin-film photovoltaic devices, in *2017 IEEE 44th Photovoltaic Specialist Conference, PVSC 2017* (2017), pp. 738–741
47. G.C.Y. Peng, M. Alber, A. Buganza Tepole, W.R. Cannon, S. De, S. Dura-Bernal, K. Garikipati, G. Karniadakis, W.W. Lytton, P. Perdikaris, L. Petzold, E. Kuhl, Multiscale modeling meets machine learning: what can we learn? *Arch. Comput. Methods Eng.* **28**, 1017–1037 (2021)

Cite this article as: J r emy Dumoulin, Emmanuel Drouard, Mohamed Amara, A fully coupled opto-electro-thermal model to investigate silicon solar cells under real operating conditions, *EPJ Photovoltaics* **13**, 20 (2022)